Journal of Materials Chemistry A

Accepted Manuscript

ROYAL SOCIETY OF CHEMISTRY

www.rsc.org/materialsA

Journal Name

ARTICLE

CeO_x-Modified RhNi Nanoparticles Grown on rGO as Highly Efficient Catalysts for Complete Hydrogen Generation from Hydrazine Borane and Hydrazine

Received 00th January 20xx,
Accepted 00th January 20xx

DOI: 10.1039/x0xx00000x

www.rsc.org/

Zhujun Zhang, Zhang-Hui Lu,* Hongliang Tan, Xiangshu Chen,* Qilu Yao

CeO_x-modified RhNi nanoparticles (NPs) grown on reduced graphene oxide (rGO) (RhNi@CeO_x/rGO) have been facilely prepared and successfully applied as highly efficient catalyst for the rapid and complete hydrogen generation from aqueous solution of hydrazine borane ($N_2H_4BH_3$) and hydrazine (N_2H_4), respectively. It was found that the CeO_x-doped RhNi NPs with a size of around 3.5 nm were highly dispersed on rGO nanosheet. Among all the catalysts investigated, the optimized catalyst $Rh_{0.8}Ni_{0.2}$@CeO_x/rGO with CeO_x content of 13.9 mol% exhibited the highest catalytic performance. The total turnover frequency (TOF) of $Rh_{0.8}Ni_{0.2}$@CeO_x/rGO for hydrogen generation from $N_2H_4BH_3$ reached 666.7 h^{-1} ($mol_{H_2}{\cdot}mol_{(Rh+Ni)}^{-1}{\cdot}h^{-1}$) at 323 K, which was among the highest of all the catalysts reported to date for this reaction, 10-fold higher than the benchmarked catalyst $Rh_{0.8}Ni_{0.2}$, 3-fold higher than $Rh_{0.8}Ni_{0.2}$ with CeO_x dopant ($Rh_{0.8}Ni_{0.2}$@CeO_x) and rGO support ($Rh_{0.8}Ni_{0.2}$/rGO). Even at room temperature, $Rh_{0.8}Ni_{0.2}$@CeO_x/rGO can achieve a complete hydrogen generation from $N_2H_4BH_3$ and N_2H_4 with a TOF value of 111.2 and 36.4 h^{-1}. This excellent catalytic performance might be attributed to the synergistic structural and electronic effect of RhNi NPs, CeO_x dopant, and rGO support. Moreover, this general method can be easily extended to facile synthesis of other metal/rGO systems with the doping of rare-earth oxides for more applications.

Introduction

The search for effective on-board hydrogen storage materials with the combination of high gravimetric/volumetric hydrogen density and appropriate kinetics remains one of the most challenging barriers on the road to a "hydrogen economy" society.[1-5] Recent developments in this direction have suggested hydrazine borane ($N_2H_4BH_3$) and hydrazine (N_2H_4) as the promising materials for hydrogen storage.[6] Hydrazine borane, a stable and safe solid at room temperature having hydrogen content as high as 15.4 wt%, can be prepared by a reaction of hydrazine hemisulfate with sodium borohydride in dioxane.[7-16] A promising approach for complete H_2 generation from $N_2H_4BH_3$ is by hydrolysis of the BH_3 group and selective decomposition of the N_2H_4 moiety of $N_2H_4BH_3$ to H_2 and N_2 (Eq. (1) and (2)),[10] corresponding to a theoretical gravimetric hydrogen storage capacity (GHSC) of 10.0 wt% for the system $N_2H_4BH_3$–$3H_2O$. Hydrazine (N_2H_4), which is a liquid over a wide range of temperatures (219-392 K), is considered as a promising liquid chemical hydrogen storage material because of its high GHSC of (8.0 wt %), simple byproduct (N_2) and safe handling.[17-35] The theoretical GHSC of $N_2H_4BH_3$ or N_2H_4 is higher than these of benchmarked hydrogen storage systems $NaBH_4$–$4H_2O$ (7.3 wt %) and NH_3BH_3–$4H_2O$ (5.9 wt %).[6] In order to maximize the efficacy of $N_2H_4BH_3$ or N_2H_4 as a hydrogen storage material, the incomplete decomposition of N_2H_4 to NH_3 by another pathway Eq. (3) should be avoided. A number of noble and non-noble metal based bi-metallic catalysts have recently been developed and applied in these reactions. However, most of these catalysts show a poor activity and reusability,[36,37] which will limit their further application. Accordingly, the search for novel heterogeneous catalysts with enhanced catalytic performance for NH_3-free H_2 production from $N_2H_4BH_3$ or N_2H_4 is of current research interest.

$$N_2H_4BH_3(s) + 3H_2O(l) \rightarrow N_2H_4(l) + H_3BO_3(l) + 3H_2(g) \quad (1)$$

$$N_2H_4(l) \rightarrow N_2(g) + 2H_2(g) \quad (2)$$

$$3N_2H_4(l) \rightarrow 4NH_3(g) + N_2(g) \quad (3)$$

Recent studies demonstrated that the catalytic activity of nickel-based catalysts could be greatly enhanced by doping with a small amount of cerium oxide.[38-45] For example, in contrast to pure Ni NPs, the Ni NPs modifying with a small amount of CeO_2 displayed a 3-fold increase of TOF and an enhancement of hydrogen selectivity from 67% to 99% for hydrogen generation from N_2H_4 aqueous solution.[46] Besides,

[a] Jiangxi Inorganic Membrane Materials Engineering Research Centre, College of Chemistry and Chemical Engineering, Jiangxi Normal University, Nanchang 330022, China. Email: luzh@jxnu.edu.cn; cxs66cn@jxnu.edu.cn

Electronic Supplementary Information (ESI) available: Experimental details for synthesis $N_2H_4BH_3$; XRD, Raman, FTIR, XPS, MS and NMR patterns. See DOI: 10.1039/x0xx00000x

we found that an amorphous $Ni_{0.9}Pt_{0.1}$-CeO_2 NPs displayed a much higher activity than that of $Ni_{0.9}Pt_{0.1}$ NPs without CeO_2 for hydrogen generation from $N_2H_4BH_3$.[47] Yet, to maximize the catalytic activity and stability of the active metal NPs, a suitable support is required to well immobilize and disperse the active NPs. Owing to its inherent advantages such as fantastic thermal/electrical conductivity, light weight, excellent flexibility, and mechanical strength, reduced graphene oxide (rGO) has been applied as an ideal substrate for high-performance catalysts.[48-50] The anchoring of NPs on rGO nanosheet could be capable of facilitating the electron transfer and mass transport kinetics during the catalytic reaction process. In this case, the combination of cerium oxide, rGO and active metal NPs may lead to an enhanced catalytic activity as well as selectivity and stability during the catalytic process.

Herein, CeO_x-doped RhNi NPs anchored on rGO nanosheet (RhNi@CeO_x/rGO) were successfully prepared via a one-step co-reduction approach. The rGO nanosheet was proved to be a distinct support and effective dispersing agent for anchoring the RhNi@CeO_x NPs, while the doping of amorphous CeO_x could decrease the crystallinity of RhNi alloy NPs. In comparison with the pure $Rh_{0.8}Ni_{0.2}$ alloy NPs, $Rh_{0.8}Ni_{0.2}$@CeO_x and the $Rh_{0.8}Ni_{0.2}$/rGO catalysts, the obtained $Rh_{0.8}Ni_{0.2}$@CeO_x/rGO nanocomposites (NCs) exhibits a much higher catalytic activity and prominent stability for selective hydrogen generation from $N_2H_4BH_3$ or N_2H_4 aqueous solution without NH_3 impurity.

Experimental

Materials

Sodium borohydride ($NaBH_4$, 98%), 1, 4-dioxane (99.8%) and cerium (III) nitrate hexahydrate ($Ce(NO_3)_3{\cdot}6H_2O$, 99.5%) were purchased from J&KCHEMICAL®. Rhodium chloride hydrate ($RhCl_3{\cdot}3H_2O$, 99.95%) and hydrazine monohydrate ($N_2H_4{\cdot}H_2O$, 98.0%) were bought from Alladin. Hydrazine hemisulfate salt ($N_2H_4{\cdot}1/2H_2SO_4$) and n-pentane (99.5%) were obtained from Sigma Aldrich. Nickel (II) chloride hexahydrate ($NiCl_2{\cdot}6H_2O$, ⩾ 98.0%), sodium hydroxide (NaOH, ⩾96.0%), and hydrochloric acid (HCl, 36%~37%) were provided by Sinopharm Chemical Reagent Co., Ltd. Hexadecyltrimethylammonium bromide-aided (CTAB, $CH_3(CH_2)_{15}N(Br)(CH_3)_3$, ⩾ 96.0%), myristyltrimethylammonium bromid (TTAB, $C_{17}H_{38}BrN$) and polyvinylpyrrolidone (PVP) was got from Fluka. All chemicals were used as obtained. We use ordinary distilled water as the reaction solvent. The synthesis and characterization of $N_2H_4BH_3$ (>99%) have been described in our previous paper.[47,50,51]

Synthesis of catalysts

The RhNi@CeO_x/rGO NCs were facilely prepared by co-reduction of graphene oxide (GO) and the metal precursors using sodium borohydride as a reducing agent. In a typical synthetic procedure, 5 mL aqueous solution containing 10 mg of GO synthesized by a modified Hummers method[48-50] and 15 mg of CTAB were ultrasoniced for 5 min to fully homogenize the contents. Then, 4.8 mg of $NiCl_2{\cdot}6H_2O$, 16.74 mg of $RhCl_3{\cdot}3H_2O$ and 7.0 mg of $Ce(NO_3)_3{\cdot}6H_2O$ were added to the above suspension. The suspension was under vigorous magnetic stirring for 60 min. After that, 30 mg of $NaBH_4$ was quickly poured into the reactor under rapid magnetic stirring for 20 min, resulting in the generation of $Rh_{0.8}Ni_{0.2}$@CeO_x/rGO (13.9 mol% Ce) NCs as a black suspension, which was then directly used for the catalytic reactions. The synthesis of RhNi@CeO_x/rGO NCs with different bimetallic compositions (Ni, $Rh_{0.1}Ni_{0.9}$, $Rh_{0.3}Ni_{0.7}$, $Rh_{0.5}Ni_{0.5}$, $Rh_{0.7}Ni_{0.3}$, $Rh_{0.9}Ni_{0.1}$, Rh) are following the above process by changing the initial molar ratio of metal salts. To discuss the effect of Ce, the $Rh_{0.8}Ni_{0.2}$@CeO_x/rGO NCs with different molar content of Ce (Ce/(Rh+Ni+Ce) = 7.5, 13.9, 18.7, 24.4 and 31.6 mol%) were also prepared by the same method by altering the initial amount of $Ce(NO_{3)3}{\cdot}6H_2O$ (3.5, 7.0, 10.0, 14.0 and 20.0 mg). The $Rh_{0.8}Ni_{0.2}$/rGO, $Rh_{0.8}Ni_{0.2}$@CeO_x, $Rh_{0.8}Ni_{0.2}$, rGO and CeO_x samples were also synthesized by the same methods.

Catalysts characterization

The crystal phase properties of the synthesized nanocatalysts were analyzed with a Rigaku RINT-2200 X-ray diffractometer (XRD) using Cu Kα radiation at 40 kV and 40 mA. The morphologies and sizes of the samples were determined by using a transmission electron microscope (TEM, Tecnai G2 F20) equipped with energy dispersed X-ray detector (EDX) for elemental analysis. One or two droplets of the synthesized catalyst suspension were deposited on a carbon coated copper grid for the TEM characterization. Atomic Force Microscopy (AFM) measurements were carried on a FSM-Precision FM-Nanoview 1000 AFM. The specific surface area measurements were performed with N_2 adsorption/desorption isotherms at liquid nitrogen temperature (77 K) after dehydration under vacuum at 100 °C for 8 h using BELSORP-mini II. Raman spectra were collected with a confocal Raman microscope (LabRAM HR). FTIR spectra were carried out at room temperature by using a Thermo Nicolet 870 instrument using KBr discs in the 500-4000 cm^{-1} region. X-ray photoelectron spectroscopy (XPS) measurements were performed with a Thermo scientific ESCALAB 250 multifunctional imaging electron spectrometer. Mass analysis of the generated gases from $N_2H_4BH_3$ over $Rh_{0.8}Ni_{0.2}$@CeO_x/rGO was performed using a Balzers Prisma QMS 200 mass spectrometer.

Catalytic reactions

The catalytic activity of the as-synthesized RhNi@CeO_x/rGO, $Rh_{0.8}Ni_{0.2}$/rGO, $Rh_{0.8}Ni_{0.2}$@CeO_x, $Rh_{0.8}Ni_{0.2}$, rGO and CeO_x towards hydrogen release from aqueous solution of $N_2H_4BH_3$ or N_2H_4 was evaluated in a typical water-filled graduated burette system. Typically, the reactor containing the catalyst suspension and NaOH (0.5 M) is placed in a water bath thermostated at 50 °C and connected to a water-filled inverted burette. A trap filled with HCl (0.1 M) solution is placed between the reactor and the inverted burette to eliminate the influence of any evolving ammonia (NH_3). The flask is well sealed with a silicon septum. To start the catalytic reaction, $N_2H_4BH_3$ or $N_2H_4{\cdot}H_2O$ ($n(Rh+Ni)/n(N_2H_4BH_3)$ or $n(N_2H_4)$=0.1) is added into the reactor and the volume of H_2 along N_2 is

measured, from which the molar ratio $\lambda = n(H_2+N_2)/n(N_2H_4BH_3)$ or $\gamma = n(H_2+N_2)/n(N_2H_4)$ can be obtained. The selectivity (α) for hydrogen generation from $N_2H_4BH_3$ can evaluated on the basis of the equation: $N_2H_4BH_3 + 3H_2O \rightarrow B(OH)_3 + (3+2\alpha)H_2 + (2\alpha+1)/3N_2 + 4(1-\alpha)/3NH_3$, which could be deduced from the equations (1), (2) and (3). Therefore, the selectivity is defined as Eq. (4). The selectivity towards H_2 generation from decomposition of N_2H_4 (β) can be calculated by using Eq. (5).

$$\alpha = \frac{3\lambda - 10}{8} \quad \left(\lambda = \frac{n(H2+N2)}{n(N2H4BH3)};\ \frac{10}{3} \ll \lambda \ll 6\right) \tag{4}$$

$$\beta = \frac{3\gamma - 1}{8} \quad \left(\gamma = \frac{n(H2+N2)}{n(N2H4)};\ \frac{1}{3} \ll \gamma \ll 3\right) \tag{5}$$

Durability and reusability test

The durability of the $Rh_{0.8}Ni_{0.2}@CeO_x$/rGO NCs was tested: after the first cycle of hydrogen generation reaction was completed, another equivalent of $N_2H_4BH_3$ or $N_2H_4{\cdot}H_2O$ was added into the reaction system and the gas released was monitored by the gas burette. It should be noted that an excess amount of NaOH (2.0 M) was used in this recycle test for hydrogen generation from $N_2H_4BH_3$, due to the neutralization of NaOH by the hydrolysate (H_3BO_3) reuslted from the first step ($-BH_3$ hydrolysis) of $N_2H_4BH_3$ dehydrogenation reaction.[50] The reactions were repeated for six runs under the same conditions as the first cycle. Then, the catalyst was separated from the reaction solution by centrifugation, washed by water and recycled for the same catalytic reactions under the same conditions.

Results and discussion

Synthesis and characterization of catalysts

The CeO_x-doped RhNi alloy NPs were facilely grown on rGO nanosheet via a one-step co-reduction approach (Scheme 1). Typically, the metal salts with different molar ratio were firstly impregnated on GO nanosheets with the help of magnetic stirring and CTAB. To our knowledge, $Ce(NO_3)_3$ is very unstable in alkaline solution and can be easily hydrolyzed to $Ce(OH)_3$, then the redox reaction between $Ce(OH)_3$ and Rh^{3+} or O_2 will lead to the formation of CeO_x (eqn. (S1) and (S2)).[52] Here, $NaBH_4$ serve as a reducing agent for the reduction of metal salt and GO, while the hydrolysate ($NaB(OH)_4$) of $NaBH_4$ provided the alkaline environment for the formation of CeO_x. As the amorphous CeO_x and RhNi alloy may be formed almost simultaneously, the formed RhNi or CeO_x served as the in situ

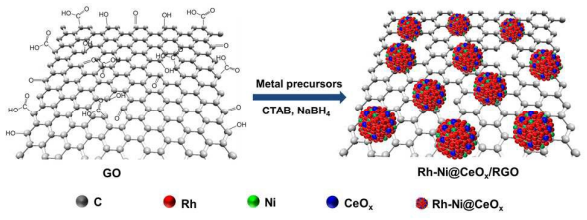

Scheme 1 Schematic illustration of preparation of the RhNi@CeO_x/rGO NCs.

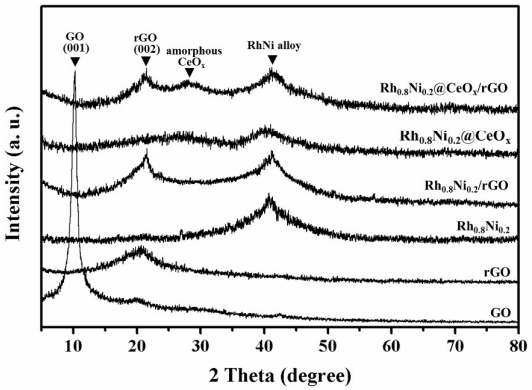

Fig. 1 Powder XRD patterns of the obtained GO, rGO, $Rh_{0.8}Ni_{0.2}$, $Rh_{0.8}Ni_{0.2}$/rGO, $Rh_{0.8}Ni_{0.2}@CeO_x$ and $Rh_{0.8}Ni_{0.2}@CeO_x$/rGO samples.

seeds for the successive growth of RhNi@CeO_x hybrid NPs. CTAB plays a role as a dispersing agent and stabilizer for the synthesis of uniform RhNi@CeO_x/rGO. The synthesized RhNi@CeO_x/rGO NCs were used as catalysts for hydrogen release from $N_2H_4BH_3$ or N_2H_4 aqueous solution. The $Rh_{0.8}Ni_{0.2}@CeO_x$/rGO NCs exhibited the highest activity among all the samples tested (vide infra), and therefore, were chosen as the model catalyst for full instrument characterization.

The synthesized nanocatalysts were isolated by centrifugation from the reaction solution, washed by water and following dried in vacuum oven for characterization experiments. The powder XRD patterns of $Rh_{0.8}Ni_{0.2}@CeO_x$/rGO, $Rh_{0.8}Ni_{0.2}$/rGO, $Rh_{0.8}Ni_{0.2}@CeO_x$, $Rh_{0.8}Ni_{0.2}$, rGO, and GO are shown in Fig. 1. The most intense peak at around 2θ = 10.2° corresponding to the (001) reflection of GO disappeared at the rGO and rGO-containing samples, and a new peak at around 2θ = 21.4° was observed, indicating that GO was successfully reduced to rGO during the synthetic process. As shown in Fig. 1, all the RhNi containing samples ($Rh_{0.8}Ni_{0.2}$, $Rh_{0.8}Ni_{0.2}$/rGO, $Rh_{0.8}Ni_{0.2}@CeO_x$ and $Rh_{0.8}Ni_{0.2}@CeO_x$/rGO) exhibited a crystalline peak centered at around 2θ = 41.2°, which was between the fcc (111) diffraction peaks of Rh (PDF#05-0685) and Ni (PDF#04-0850), indicating the formation of RhNi alloy. In addition, the CeO_x-doped samples ($Rh_{0.8}Ni_{0.2}@CeO_x$ and $Rh_{0.8}Ni_{0.2}@CeO_x$/rGO) showed a broad and weak peak at around 2θ = 28.2°, which can be assigned to the amorphous state of CeO_x. In particular, these samples displayed a weaker RhNi alloy signal than these of the samples without the doping of CeO_x ($Rh_{0.8}Ni_{0.2}$ and $Rh_{0.8}Ni_{0.2}$/rGO), which probably due to the fact that the doping of amorphous CeO_x into the ultrafine nanocrystalline of $Rh_{0.8}Ni_{0.2}$ can disturb the long-range order of the $Rh_{0.8}Ni_{0.2}$ nanoalloy and thus decrease its crystallinity. Furthermore, the formed RhNi alloy are inclined to bind more strongly to the distortions and vacancies of the amorphous CeO_x.[33] As a result, the ligand and strain effect around these sites may further lead to the disorder of the RhNi nanoalloy, and finally decrease the crystallinity of bimetal NPs. Besides, from the powder XRD patterns of RhNi@CeO_x/rGO NCs with different molar content

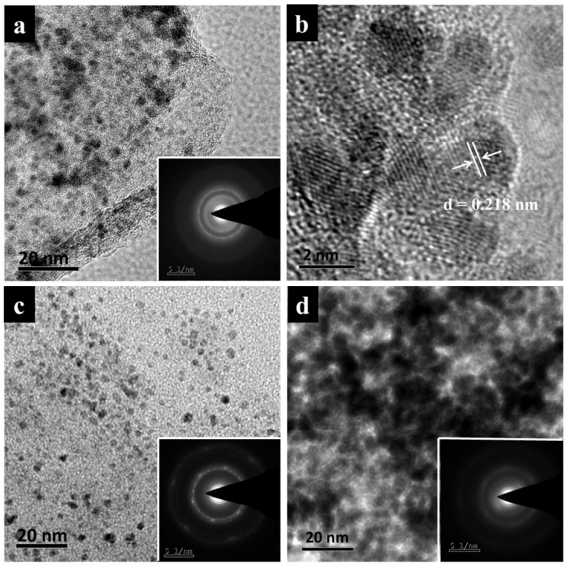

Fig. 2 TEM images and the corresponding SAED patterns (inset) for (a) $Rh_{0.8}Ni_{0.2}@CeO_x/rGO$, (c) $Rh_{0.8}Ni_{0.2}/rGO$ and (d) $Rh_{0.8}Ni_{0.2}@CeO_x$; (b) The high-resolution TEM image of $Rh_{0.8}Ni_{0.2}@CeO_x/rGO$.

of Rh (Fig. S1), it was found that the samples with Rh content ranging from 0 to 30 mol% (sample a, b and c) were in amorphous state, whereas the samples with a higher content of Rh (50-100 mol%, sample d, e, f and g) showed a weak crystalline peak of RhNi alloy or Rh. Herein, we believed that the doping of amorphous CeO_x can effectively transform the crystalline of Ni based bimetallic NPs with a small quantity of noble-metal containing to the amorphous state, as reported before for $Ni_{0.9}Pt_{0.1}$-CeO_x,[33,47] and can also effectively decrease the crystallinity of Ni-based bimetallic NPs with a majority of noble-metal containing. The RhNi NPs in amorphous state or with a low degree of crystallinity have the features of short-range order and long-rang disorder, and both these features might contribute to enhance their catalytic performance.

The morphologies and size of the synthesized $Rh_{0.8}Ni_{0.2}@CeO_x/rGO$, $Rh_{0.8}Ni_{0.2}@CeO_x$ and $Rh_{0.8}Ni_{0.2}/rGO$ were characterized by TEM and selected-area electron diffraction (SAED) (Fig. 2). As for the $Rh_{0.8}Ni_{0.2}@CeO_x/rGO$ NCs, all the metallic NPs were highly dispersed on the rGO nanosheet with average particle size of around 3.5 nm (Fig. 2a and Fig. S2). Similar particle size and dispersity were observed in $Rh_{0.8}Ni_{0.2}/rGO$ NCs (Fig. 2c), thus illustrating that the doping of $Rh_{0.8}Ni_{0.2}/rGO$ with CeO_x did not influence the distribution and growth of $Rh_{0.8}Ni_{0.2}$ NPs. However, the $Rh_{0.8}Ni_{0.2}@CeO_x$ NPs prepared without GO were aggregated to a bigger size (about 5 nm), as shown in Fig. 2d. This is understandable because the hydrophilic phenyl epoxide and hydroxyl group and the hydrophobic basal plane of GO play a role as a surfactant, which can effectively anchor the metal NPs in special areas and thus control their distribution and agglomeration on the rGO nanosheet during the synthesis process.[50,53] The high resolution TEM image of $Rh_{0.8}Ni_{0.2}@CO_x/rGO$ (Fig. 2b) shows that the metal NPs are in crystalline state with a d-spacing of 0.218 nm, which differs from the fcc (111) plane of Rh (0.228) and Ni (0.214 nm), and thus further confirms the formation of RhNi alloy. The corresponding SAED patterns show that the CeO_x-doped samples ($Rh_{0.8}Ni_{0.2}@CeO_x$ and $Rh_{0.8}Ni_{0.2}@CeO_x/rGO$) exhibit a lower degree of crystallinity (inset of Fig. 2a and 2d) than that of the sample without CeO_x ($Rh_{0.8}Ni_{0.2}/rGO$) (inset of Fig. 2c), which is in agreement with the powder XRD results (Fig. 1). The high-angle annular dark-field scanning transmission electron microscopy (HADDF-STEM) and the elemental mapping images for $Rh_{0.8}Ni_{0.2}@CeO_x/rGO$ (Fig. 3a and b) show that the metallic elements Rh, Ni, and Ce are homogeneous dispersed in these NPs. Furthermore, the energy-dispersive X-ray spectroscopy (EDX) spectrum further confirms the existence of Rh, Ni and Ce elements (Fig. S3). The atomic ratio for Rh:Ni:Ce was detected by ICP-AES (shown in Table S1), quite close to their initial contents.

The GO used for the synthesis of catalysts was characterized by using AFM measurement. The AFM results show that the average thickness of the GO nanosheets is about 1.25 nm (Fig. S4), suggesting 2-4 layers of GO. Fig. S5 shows

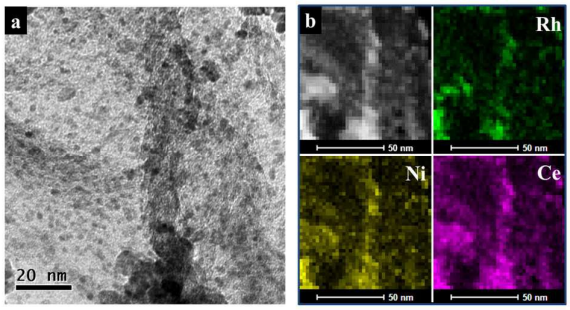

Fig. 3 (a) TEM image of $Rh_{0.8}Ni_{0.2}@CeO_x/rGO$; (b) HADDF-STEM and the EDX mapping images of $Rh_{0.8}Ni_{0.2}@CeO_x/rGO$.

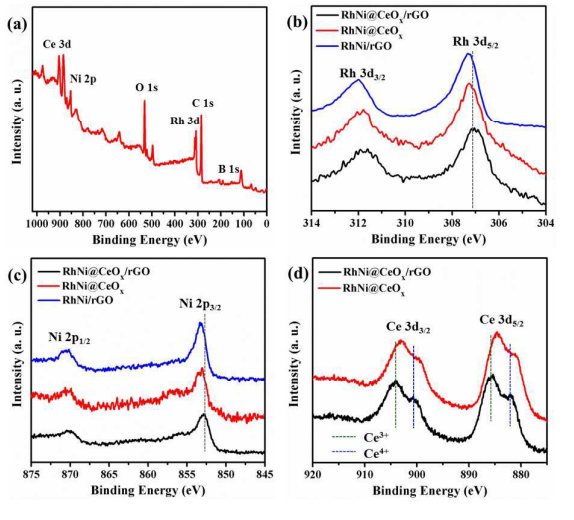

Fig. 4 (a) The survey XPS spectrum of $Rh_{0.8}Ni_{0.2}@CeO_x/rGO$ NCs; XPS spectra of (b) Rh 3d and (c) Ni 2p and (d) Ce 3d for the synthesized catalysts.

the Raman and FTIR spectra of GO and $Rh_{0.8}Ni_{0.2}@CeO_x$/rGO. It can be seen from Raman spectra (Fig. S5a) that the as-synthesized GO and $Rh_{0.8}Ni_{0.2}@CeO_x$/rGO both exhibit two peaks centered at 1335 and 1597 cm^{-1}, corresponding to the D and G bands of carbon products, respectively.[54] The intensity ratio of the D to G band (I_D/I_G) of GO is increased from 1.02 to 1.21 after loading of the $Rh_{0.8}Ni_{0.2}@CeO_x$ NPs. The relative changes in I_D/I_G is due to the increase in the number of smaller graphene domains after reduction of GO.[55] As shown in FTIR spectra of GO and $Rh_{0.8}Ni_{0.2}@CeO_x$/rGO (Fig. S5b), it can be seen clearly that the C=O peak at 1735 cm^{-1}, the C-OH peak at 1224 cm^{-1} and the C-O peak at 1053 cm^{-1} of GO disappeared after loading of $Rh_{0.8}Ni_{0.2}@CeO_x$ NPs, further indicating that the GO was reduced to rGO during the synthetic process. Additionally, the XPS results for C 1s show that the intensities of the oxygen containing functional groups (such as –C-O, -C=O, -COO) of GO (Fig. S6) decrease significantly after the formation of $Rh_{0.8}Ni_{0.2}@CeO_x$/rGO,[56] which also indicates the reduction of GO.

XPS analyses after Ar sputtering for RhNi@CeO_x/rGO, RhNi@CeO_x and RhNi/rGO were also performed to understand the electronic states and surface interaction among Rh, Ni, Ce, and rGO. The characteristic signals of metal state of Rh and Ni and CeO_x were detected from the sample of RhNi@CeO_x/rGO. The signals corresponding to Rh^0 in the Rh $3d_{5/2}$ and $3d_{3/2}$ levels appear at the binding energies (BEs) of 307.1 and 311.9 eV, respectively (Fig. 4b). And the signals for Ni^0 can be detected in the Ni $2p_{3/2}$ and Ni $2p_{1/2}$ levels with BEs of 852.8 and 870.1 eV, respectively (Fig. 4c). In addition, it can be seen from the Ce 3d level that both signals of Ce^{3+} and Ce^{4+} are found (Fig. 4d). This is probably due to the fact that the oxygen defect structure of cerium oxide is dynamic and may change spontaneously in response to physical parameters such as temperature, presence of other ions, and partial pressure of oxygen.[57] The XPS spectra show that there is a negative shift in the BEs of Rh $3d_{5/2}$ and Ni $2p_{3/2}$ of RhNi@CeO_x/rGO NCs as compared to those of the RhNi@CeO_x and RhNi/rGO NCs; whereas a positive shift of the corresponding BE of Ce $3d_{5/2}$ is observed relative to that of Ce_2O_3 and CeO_2. These shifts in BEs demonstrate that CeO_x and rGO nanosheets in the RhNi@CeO_x/rGO NCs both act as electron donors for atoms of Rh and Ni. Such electronic transport between RhNi, CeO_x, and rGO in the RhNi@CeO_x/rGO NCs might enhance their catalytic activity for $N_2H_4BH_3$ and N_2H_4 dehydrogenation. No obvious signal of B was detected by the survey XPS spectrum of $Rh_{0.8}Ni_{0.2}@CeO_x$/rGO (Fig. 4a). The high resolution of B 1s for both the RhNi@CeO_x/rGO, RhNi@CeO_x and RhNi/rGO samples show a week signal at around 192.4 eV of oxidized boron (Fig. S7), probably due to a very small residual hydrolysate of $NaBH_4$ in the samples. As no elemental B or Ni-B or Rh-B signals were observed from B 1s spectrum, we therefore infer that there is no or negligible electronic synergistic effect between B, Ni and Rh.

In this work, CTAB plays a role as a dispersing agent and stabilizer for preparing the uniform RhNi@CeO_x/rGO NCs. The TEM images (Fig. S8d) show that rGO supported RhNi@CeO_x NPs prepared by using a high concentration of CTAB (35 mg) or without CTAB have a bigger particle size (Fig. S8a), as compared to that of samples prepared by using a low concentration of CTAB (7.5-15mg) (Fig. S8b and c). The high CTAB concentrations may hinder the impregnation of metal precursors onto GO nanosheets and finally resulting in the generation of ununiform RhNi@CeO_x particles with poor dispersity on rGO nanosheets (Fig S8d). From the XRD patterns of the samples prepared with high CTAB concentrations (25-35 mg), the diffraction peaks of CTAB are also observed (Fig. S9), thus indicating the rGO nanosheets and the active metal NPs could be coated by CTAB. Other surfactants, such as PVP and TTAB, can also be used for the synthesis of RhNi@CeO_x/rGO NCs with similar compositions and particle sizes as confirmed by their XRD patterns and TEM images (Fig. S10). Besides, the influence of different stirring time (0.5-6 h) during the preparation of RhNi@CeO_x/rGO NCs is not so distinct (Fig. S11). Only the sample prepared without stirring during the impregnation period show a degree of agglomeration in certain areas of the TEM image (Fig. S11a). The RhNi@CeO_x/rGO NCs prepared in different conditions, such as different CTAB concentrations and stirring time, have a similar and low specific surface area of around 25 m^2g^{-1} (Fig. S12). It is hard to reflect the real specific surface area of RhNi@CeO_x/rGO NCs as prepared in the reaction solution, probably due to the overlapping of graphene sheets within the self-aggregation during the drying process. To examine the magnetism of the $Rh_{0.8}Ni_{0.2}@CeO_x$/rGO, we have directly using a magnet to contact the flask containing the catalyst suspension. However, the catalyst suspension was still uniformly dispersed even after 6 hours (Fig. S13), indicating that these catalysts with a low content of Ni have no or only a negligible magnetism.

Catalytic performance

Recent research have shown that the hydrogen selectivity for decomposition of N_2H_4 can be promoted in the presence of NaOH, which can not only accelerate the rate-determining deprotonation step ($N_2H_4 \rightarrow N_2H_3$*) (thus promoting reaction kinetics), but can also restrain the generation of the basic byproduct NH_3.[6,47,50] The optimum concentration of NaOH for hydrogen generation from $N_2H_4BH_3$ (200 mM, 5 mL) in the presence of $Rh_{0.8}Ni_{0.2}@CeO_x$/rGO was determined to be 0.5 M (Fig. S14). The catalytic performance of the catalyst was evaluated based on the volumetric and reaction time measurement of the amount of gases released during the reaction. As shown in Fig. 5, the catalytic performances of the $Rh_{0.8}Ni_{0.2}$, $Rh_{0.8}Ni_{0.2}$/rGO, $Rh_{0.8}Ni_{0.2}@CeO_x$ and $Rh_{0.8}Ni_{0.2}@CeO_x$/rGO nanocatalysts have been investigated for hydrogen generation from $N_2H_4BH_3$ (0.5 M NaOH) at 323 K. The pure $Rh_{0.8}Ni_{0.2}$ NPs can only generate 5.4 equiv. (H_2+N_2) per $N_2H_4BH_3$ (λ = 5.4, α = 77.5%) in about 43 min. After the $Rh_{0.8}Ni_{0.2}$ NPs were immobilized on the rGO support or doped with the amorphous CeO_x, the catalytic activity and hydrogen selectivity were enhanced greatly, with which 6.0 and 5.8 equiv. (H_2+N_2) per $N_2H_4BH_3$ (α = 100% and 93.6%) released in only 14.5 and 12.8 min, respectively. Clearly, the rGO support or the CeO_x dopant was inactive for this reaction (Fig. S15). The

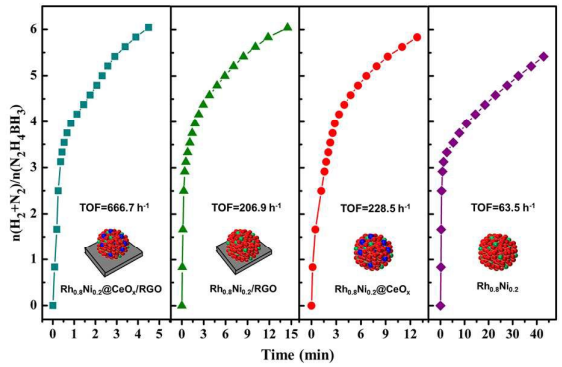

Fig. 5 Time course plots for H_2 generation from $N_2H_4BH_3$ (200 mM, 5 mL) over $Rh_{0.8}Ni_{0.2}@CeO_x$/rGO, $Rh_{0.8}Ni_{0.2}$/rGO, $Rh_{0.8}Ni_{0.2}@CeO_x$, and $Rh_{0.8}Ni_{0.2}$ catalysts (13.9 mol% Ce; $n(Ni+Rh)/n(N_2H_4BH_3)$ = 0.1) with NaOH (0.5 M) at 323 K. (inset) The structure simulation of the catalyst and corresponding total TOF value of H_2.

enhanced catalytic performance of $Rh_{0.8}Ni_{0.2}$ NPs grown on rGO can be reasonable due to the combined effect of excellent dispersion and the intimate interaction derived from rGO. In addition, the $Rh_{0.8}Ni_{0.2}$ alloy NPs modified by amorphous CeO_x shows a very low crystallinity and thus have the high concentration of unsaturated coordination sites, which can effectively improve the catalytic activity and H_2 selectivity. Similar synergistic effects were also observed in our previous work for $Ni_{0.9}Pt_{0.1}$-CeO_2[47] and $Ni_{0.9}Pt_{0.1}$/graphene[50] in the same reaction.

Since the catalytic activity can be enhanced by the modification of bimetallic NPs with addition of CeO_x or rGO nanosheet, the combination of CeO_x dopant, rGO support, and bimetallic NPs may realize a better catalytic performance. As we expected, $Rh_{0.8}Ni_{0.2}$ NPs with the doping of amorphous CeO_x supported on rGO nanosheet ($Rh_{0.8}Ni_{0.2}@CeO_x$/rGO) showed a greatly enhanced catalytic activity towards hydrogen generation from $N_2H_4BH_3$ with 6.0 equiv. (H_2+N_2) per $N_2H_4BH_3$ (λ = 6.0, α = 100%) released in only 4.5 min. The H_2/N_2 ratio of the gases released from $N_2H_4BH_3$ over the $Rh_{0.8}Ni_{0.2}@CeO_x$/rGO catalyst was further confirmed by the mass spectrometric analysis (Fig. S16), indicating a 100% hydrogen selectivity. The total turnover frequency (TOF) of $Rh_{0.8}Ni_{0.2}@CeO_x$/rGO reached 666.7 h^{-1} ($mol_{H2}\cdot mol_{(Rh+Ni)}^{-1}\cdot h^{-1}$), which was 10-fold higher than the benchmarked catalyst $Rh_{0.8}Ni_{0.2}$, 3-fold higher than $Rh_{0.8}Ni_{0.2}@CeO_x$ and $Rh_{0.8}Ni_{0.2}$/rGO. To the best of our knowledge, this is the highest value reported to date for this reaction at 323 K (Table S2). Even at room temperature (303 K), the $Rh_{0.8}Ni_{0.2}@CeO_x$/rGO NCs exhibited the complete hydrogen generation from $N_2H_4BH_3$ with a TOF value of 112.2 h^{-1} (vide infra). As far as we know, only one nanocatalyst ($Ni_{0.6}Pt_{0.4}$/MSC-30) has been reported to exhibit a 100% hydrogen selectivity and high activity toward complete conversion of $N_2H_4BH_3$ to hydrogen at room temperature,[6] and $Rh_{0.8}Ni_{0.2}@CeO_x$/rGO is the second one. The catalytic activity of $Rh_{0.8}Ni_{0.2}@CeO_x$/rGO for hydrogen generation from $N_2H_4BH_3$ at room temperature was lower than that of $Ni_{0.6}Pt_{0.4}$/MSC-30.

The $RhNi@CeO_x$/rGO NCs with different metal compositions have been tested for hydrogen generation from $N_2H_4BH_3$ (0.5 M NaOH) at 323 K (Fig. 6). The catalytic activity and selectivity were strongly dependent on the Rh/Ni ratio. Both monometallic $Rh@CeO_x$/rGO and $Ni@CeO_x$/rGO NCs showed a certain activity, with which 4.6 equiv. (H_2+N_2) per $N_2H_4BH_3$ released (λ = 4.6, α = 47.5%) in 3.8 and 61.0 min, respectively (Fig. 6a). All the $RhNi@CeO_x$/rGO catalysts with different bimetallic compositions exhibited a high catalytic activity and hydrogen selectivity with more than 5.6 equiv. gases released ($\lambda \geqslant 5.6$, $\alpha \geqslant 85\%$) (Fig. 6b). Especially, the $Rh_{0.8}Ni_{0.2}@CeO_x$/rGO NCs exhibited the highest catalytic activity with 100% hydrogen selectivity. The enhanced catalytic performance of the $RhNi@CeO_x$/rGO NCs demonstrates that the resulting synergistic effect between Rh and Ni induced by the so-called strain and ligand effects[58] is highly required for the complete hydrogen release from $N_2H_4BH_3$. Additionally, when the molar content of Ce is set as the present value of 13.9 mol%, the resulting $Rh_{0.8}Ni_{0.2}@CeO_x$/rGO has the optimum performance (Fig. S17). The catalytic activity of this catalyst will decrease with the decreasing or increasing the Ce content of 13.9 mol%.

The $Rh_{0.8}Ni_{0.2}@CeO_x$/rGO NCs prepared with different

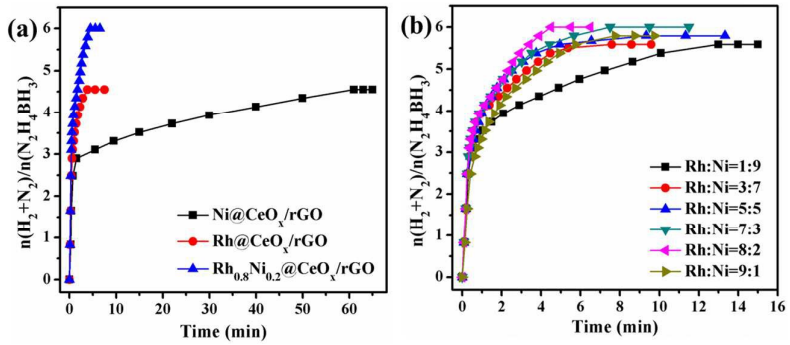

Fig. 6 Time course plots for H_2 generation from $N_2H_4BH_3$ (200 mM, 5 mL) over (a) the monometallic $Ni@CeO_x$/rGO and $Rh@CeO_x$/rGO catalysts and (b) $RhNi@CeO_x$/rGO catalysts with different molar content of Rh (13.9 mol% Ce; $n(Ni+Rh)/n(N_2H_4BH_3)$ = 0.1) in the presence of NaOH (0.5 M) at 323 K.

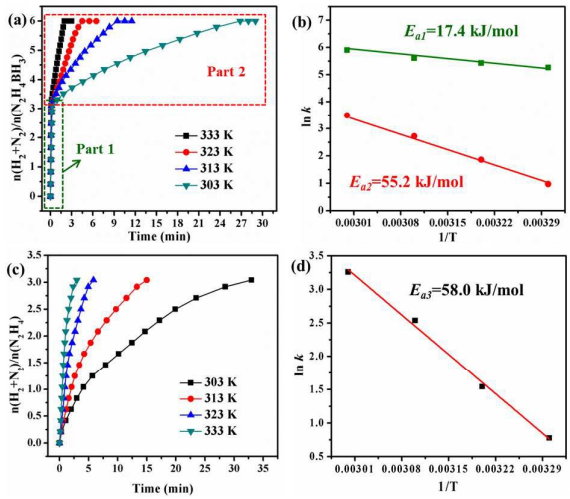

Fig. 7 Time course plots for H_2 generation from aqueous solution of (a) $N_2H_4BH_3$ and (c) N_2H_4 over $Rh_{0.8}Ni_{0.2}@CeO_x$/rGO catalysts (13.9 mol% Ce; n(Ni+Rh)/n($N_2H_4BH_3$ or N_2H_4) = 0.1) at temperatures ranging from 303 to 333 K. Plot of ln *k* versus 1/T during the releasing of H_2 from (b) hydrolysis of BH_3 (Part 1) and decomposition of the N_2H_4 moiety of $N_2H_4BH_3$ (Part 2) and (d) decomposition of N_2H_4 aqueous solution over $Rh_{0.8}Ni_{0.2}@CeO_x$/rGO at different temperatures.

CTAB concentrations were also tested for $N_2H_4BH_3$ dehydrogenation (Fig. S18a). The sample prepared without surfactant show only a little decrease of catalytic activity (TOF: 400 h^{-1}) in comparison with the samples prepared with low CTAB concentration (7.5-15mg), probably due to their relative bigger particle sizes. The samples prepared with high CTAB concentrations (25-35 mg) exhibited a decrease in catalytic activity as compared to that of sample with low CTAB concentration or without surfactant. This is likely due to the fact that the surface of the RhNi@CeO_x/rGO NCs prepared with high CTAB concentrations were coated by CTAB, and thus leading to a decrease in the number of exposed active sites. The catalysts prepared with other surfactants, such as PVP and TTAB, have a similar catalytic activity as the sample prepared with CTAB (Fig. S18b). The as-prepared catalyst showed a small decrease in the activity, after removed the CTAB by thoroughly washed by ethanol and water (Fig. S19), indicating that the rGO nanosheets supported RhNi@CeO_x NPs can be stabilized by CTAB. Besides, the stirring time during the impregnation of metal precursors has no significant influence on catalytic performance towards H_2 generation from $N_2H_4BH_3$ (Fig. S20), while only the sample prepared without stirring show a little decrease of activity. To discuss the effects of the residuals oxygen groups on rGO nanosheets, an excess amount of $NaBH_4$ was used to reduce the oxygen groups completely, which was further verified by XPS measurements (Fig. S21). In comparison with the sample with a few residual oxygen groups (Fig. S6b), the sample without oxygen groups had almost the same activity (Fig. S22), thus indicating that a few residual oxygen groups on rGO nanosheets have negligible effect on the catalytic performance in the present work.

The catalytic performance of $Rh_{0.8}Ni_{0.2}@CeO_x$/rGO NCs has also been tested for hydrogen generation from $N_2H_4BH_3$ at different temperatures (Fig. 7). The catalytic reactions for H_2 generation from $N_2H_4BH_3$ were completed in 2.0, 4.5, 9.5 and 27.0 min at 333, 323, 313 and 303 K, respectively, corresponding to TOF values of 1500.0, 666.7, 315.8 and 111.2 h^{-1} (Fig. 7a). Based on the Arrhenius plot fitted by the H_2 generation rate for the hydrolysis of BH_3 group and the decomposition of N_2H_4 moiety of $N_2H_4BH_3$ at different reaction temperatures, we can obtain the corresponding activation energy value E_{a1}=17.4 kJ/mol and E_{a2}=55.2 kJ/mol, respectively (Fig. 7b). Also, the $Rh_{0.8}Ni_{0.2}@CeO_x$/rGO catalysts with different metal concentrations (Rh+Ni: 0.005-0.025 M) were used for the same reactions (Fig. S23). As expected, the H_2 generation rate of both the hydrolysis and decomposition increases with increasing catalyst concentration. The plots based on the H_2 generation rate versus catalyst concentrations (both in logarithmic scale) show that a slope of 0.87 and 0.93 is obtained for the hydrolysis and decomposition reactions, respectively, implying that both the reactions approximate first-order kinetics with respect to the catalyst concentration. The plausible catalytic scheme of hydrazine borane dehydrogenation over the as-prepared RhNi@CeO_x/rGO is illustrated in Scheme 2. Firstly, the interaction between the $N_2H_4BH_3$ molecule and the RhNi@CeO_x surface will produce the activated complex species, who attack by a H_2O molecule readily leads to concerted dissociation of the B–N bonding of $N_2H_4BH_3$. When the BH_3 group of $N_2H_4BH_3$ is catalytically hydrolyzed by the catalysts, concurrently, the resulting N_2H_4 moieties directly interact with metal NPs to generate N_2 and H_2. The kinetic rate for the hydrolysis of the –BH_3 group is much faster than that of the decomposition of N_2H_4 moiety of $N_2H_4BH_3$.

The $Rh_{0.8}Ni_{0.2}@CeO_x$/rGO catalyst was used to catalytically decompose the same amount of N_2H_4 as that resulted from the first step of $N_2H_4BH_3$ dehydrogenation

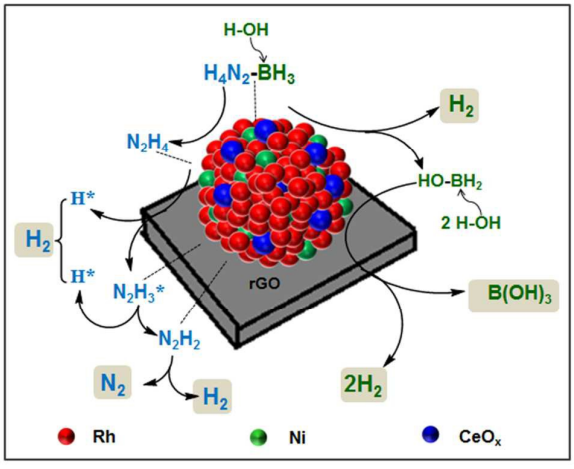

Scheme 2. Schematic representation of H_2 generation from $N_2H_4BH_3$ over $Rh_{0.8}Ni_{0.2}@CeO_x$/rGO catalysts.

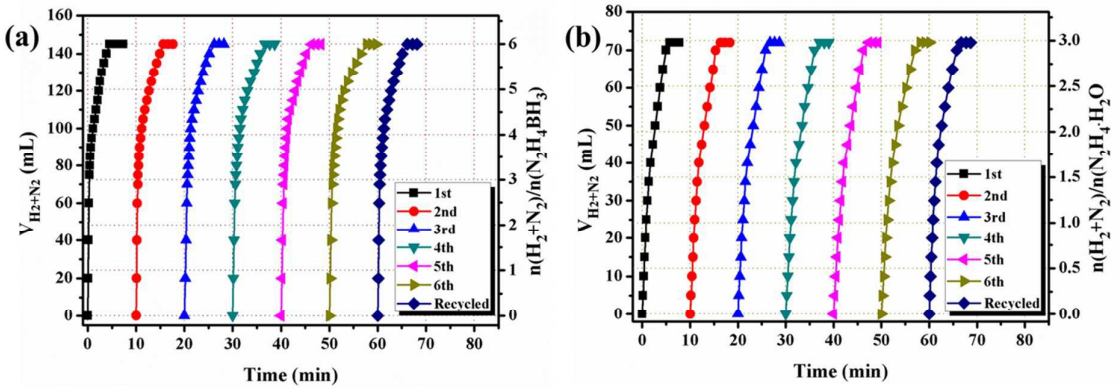

Fig. 8 Durability and reusability test for H_2 generation from aqueous solution of (a) $N_2H_4BH_3$ and (b) N_2H_4 (1.0 mmol) catalyzed by $Rh_{0.8}Ni_{0.2}@CeO_x$/rGO (n(Ni+Rh)/n($N_2H_4BH_3$ or N_2H_4) = 0.1) at 323 K.

reaction under the same conditions. The completely decomposition of N_2H_4 at 333, 323, 313 and 303 K can finish in 3.0, 5.7, 15.0 and 33.0 min in the presence of $Rh_{0.8}Ni_{0.2}@CeO_x$/rGO (Fig. 7c), corresponding to total TOF values of 400.0, 210.5, 80.0 and 36.4 h^{-1}, respectively. These TOF values were relatively high value among all the reported catalysts for the decomposition of N_2H_4 at various temperatures (Table S3).[59,60] Especially, the present catalyst can achieve a complete H_2 release from N_2H_4 at room temperature with a TOF of 36.4 h^{-1}, which was 5-fold higher than the benchmarked catalyst $Rh_{0.8}Ni_{0.2}$ in the previous literature.[36] The activation energy (E_{a3}) for decomposition of N_2H_4 catalyzed by $Rh_{0.8}Ni_{0.2}@CeO_x$/rGO was determined to be 58.0 kJ/mol (Fig. 7d), higher than that value (55.2 kJ/mol) of this catalyst for dehydrogenation of N_2H_4 moiety of $N_2H_4BH_3$. The $Rh_{0.8}Ni_{0.2}@CeO_x$/rGO NCs exhibited a lower catalytic activity for the decomposition of N_2H_4 than that for the dehydrogenation of $N_2H_4BH_3$. A plausible explanation is that when the BH_3 group of $N_2H_4BH_3$ is catalytically hydrolyzed by the catalysts (very fast), concurrently, the resulting N_2H_4 moieties directly interact with metal NPs to generate N_2 and H_2, thus promoting the kinetic properties of $N_2H_4BH_3$ dehydrogenation. Similar reaction characteristics for Rh_4Ni and $Ni_{0.6}Pt_{0.4}$/MSC-30 were observed in the previous reports.[6,37]

As the durability and reusability of catalysts is very important for practical application. In this sense, the durability and reusability of $Rh_{0.8}Ni_{0.2}@CeO_x$/rGO NCs for hydrogen generation from aqueous solution of $N_2H_4BH_3$ or N_2H_4 at 323 K were carried out. As shown in Fig. 8, after six cycles, the $Rh_{0.8}Ni_{0.2}@CeO_x$/rGO NCs showed a 100% hydrogen selectivity and productivity, but a little decrease in activity for hydrogen generation from $N_2H_4BH_3$ and N_2H_4, respectively. However, the treatment of this catalyst by washing with water leaded to the recovery of the active sites, which showed almost the same activity as the pristine catalysts for hydrogen generation from $N_2H_4BH_3$ or N_2H_4, indicating that the $Rh_{0.8}Ni_{0.2}@CeO_x$/rGO NCs had a good durability and reusability in the catalytic reactions. The good stability of the $Rh_{0.8}Ni_{0.2}@CeO_x$/rGO NCs was verified by the TEM (Fig. S24) and powder XRD characterization (Fig. S25).

Conclusions

In summary, RhNi alloy NPs with the doping of amorphous CeO_x have been successfully anchored on the surface of rGO nanosheets via a one-step co-reduction synthetic process at room temperature, and successfully applied as highly efficient catalyst for the complete hydrogen production from aqueous solution of $N_2H_4BH_3$ or N_2H_4. The TEM and XRD images showed that CeO_x and rGO can effectively decrease the crystallinity and size of RhNi NPs, respectively. The XPS results demonstrated that CeO_x and rGO nanosheets in the the RhNi@CeO_x/rGO NCs both act as electron donors for Rh and Ni. Therefore, the modification of the surface electronic structure and chemical properties of RhNi@CeO_x NPs through the strain and ligand effects among Ni, Rh, CeO_x and rGO is responsible for the high activity of the RhNi@CeO_x/rGO NCs. These synergistic structural and electronic effects are highly required for the complete hydrogen release from aqueous solution of $N_2H_4BH_3$ or N_2H_4. In comparison with the $Rh_{0.8}Ni_{0.2}$, $Rh_{0.8}Ni_{0.2}@CeO_x$, $Rh_{0.8}Ni_{0.2}$/rGO, and most of the catalysts reported to date, the obtained $Rh_{0.8}Ni_{0.2}@CeO_x$/rGO NCs exhibited a much higher catalytic activity towards hydrogen generation from $N_2H_4BH_3$ and N_2H_4 at 323 K with 100% hydrogen selectivity and outstanding durability and reusability. The catalytic results open up new avenues in the effective application of hydrazine borane and hydrazine aqueous solution as the feasible hydrogen storage materials for fuel cell applications.

Acknowledgements

This work was financially supported by National Natural Science Foundation of China (No. 21463012 and 21103074). Z.-H. Lu was supported by Young Scientist Foundation of Jiangxi

Province (20133BCB23011) and "Gan-po talent 555" Project of Jiangxi Province.

Notes and references

1 O. K. Farha, A. M. Spokoyny, K. L. Mulfort, M. F. Hawthorne, C. A. Mirkin and J. T. Hupp, *J. Am. Chem. Soc.*, **2007**, 129, 12680-12681.
2 D. Pukazhselvan, V. Kumar and S. K. Singh, *Nano Energy*, **2012**, 1, 566-589.
3 C. Fellay, P. J. Dyson and G. Laurenczy, *Angew. Chem.*, **2008**, 120, 4030-4032.
4 A. Boddien, D. Mellmann, F. Gärtner, R. Jackstell, H. Junge, P. J. Dyson, G. Laurenczy, R. Ludwig and M. Beller, *Science*, **2011**, 333, 1733-1736.
5 X. Cao, Y. Han, C. Gao, Y. Xu, X. Huang, M. Willander and N. Wang, *Nano Energy*, **2014**, 9, 301-308.
6 Q. L. Zhu, D. C. Zhong, U. B. Demirci and Q. Xu, *ACS Catal.*, **2014**, 4, 4261-4268.
7 T. Hügle, M. F. Kühnel and D. Lentz, *J. Am. Chem. Soc.*, **2009**, 131, 7444-7446.
8 T. He, H. Wu, G. Wu, J. Wang, W. Zhou, Z. Xiong, J. Chen, T. Zhang and P. Chen, *Energy Environ. Sci.*, **2012**, 5, 5686-5689.
9 R. Moury, G. Moussa, U. B. Demirci, J. Hannauer, S. Bernard, E. Petit, A. V. D. Lee and P. Miele, *Phys. Chem. Chem. Phys.*, **2012**, 14, 1768-1777.
10 J. Hannauer, O. Akdim, U. B. Demirci, C. Geantet, J. M. Herrmann, P. Miele and Xu, Q. *Energy Environ. Sci.*, **2011**, 4, 3355-3358.
11 D. Clémençon, J. F. Petit, U. B. Demirci, Q. Xu and P. Miele, *J. Power Sources*, **2014**, 260, 77-81.
12 Ç. Çakanyıldırım, U. B. Demirci, T. Şener, Q. Xu and P. Miele, *Int. J. Hydrogen Energy*, **2012**, 37, 9722-9729.
13 J. Thomas, M. Klahn, A. Spannenberg, T. Beweries, *Dalton Trans.*, **2013**, 42, 14668-14672.
14 C. Li, Y. Dou, J. Liu, Y. Chen, S. He, M. Wei, D. G. Evans and X. Duan, *Chem. Commun.*, **2013**, 49, 9992-9994.
15 S. Karahan, M. Zahmakıran and S. Özkar, *Int. J. Hydrogen Energy*, **2011**, 36, 4958-4966.
16 D. Özhava, N. Z. Kiliçaslan, S. Özkar, *Appl. Catal. B: Environ.*, **2015**, 162, 573-582.
17 J. Wang, L. Wang, Y. Wen, L. Gu and Y. Zhang, *Adv. Energy Mater.*, 10.1002/aenm.201401879.
18 J. K. Sun, Q. Xu, *ChemCatChem*, **2015**, 7, 526-531.
19 J. M. Yan, Z. L. Wang, H. L. Wang and Q. Jiang, *J. Mater. Chem.*, **2012**, 22, 10990-10993.
20 H. L. Wang, J. M. Yan, S. J. Li, X. W Zhang and Q. Jiang, *J. Mater. Chem. A*, **2015**, 3, 121-124.
21 L. He, Y. Huang, A. Wang, X. Wang, X. Chen, J. J. Delgado and T. Zhang, *Angew. Chem. Int. Ed.*, **2012**, 51, 6191-6194.
22 L. He, Y. Huang, A. Wang, Y. Liu, X. Liu, X. Chen, J. J. Delgado, X. Wang and T. Zhang, *J. Catal.*, **2013**, 298, 1-9.
23 F. Yang, Y. Z. Li, W. Chu, C. Li, D. G. Tong, *Catal. Sci. Technol.*, **2014**, 4, 3168-3179.
24 S. K. Singh, A. K. Singh, K. Aranishi and Q. Xu, *J. Am. Chem. Soc.*, **2011**, 133, 19638-19641.
25 J. Wang, Y. Li and Y. Zhang, *Adv. Funct. Mater.*, **2014**, 24, 7073-7077.
26 A.K. Singh, Q. Xu, *ChemCatChem*, **2013**, 5, 3000-3004.
27 B. Xia, N. Cao, H. Dai, J. Su, X. Wu, W. Luoa and G. Cheng, *ChemCatChem*, **2014**, 6, 2549-2552.
28 Y. Jiang, Q. Kang, J. Zhang, H. B. Dai and P. Wang, *J. Power Sources*, **2015**, 273, 554-560.
29 S-II. O, J. M. Yan, H. L. Wang, Z. L. Wang and Q. Jiang, *J. Power Sources*, **2014**, 262, 386-390.
30 W. Gao, C. Li, H. Chen, M. Wu, S. He, M. Wei, D. G. Evans and X. Duan, *Green Chem.*, **2014**, 16, 1560-1568.
31 L. He, Y. Huang, X. Y. Liu, L. Li, A. Wang, X. Wang, C. Y. Mou and T. Zhang, *Appl. Catal. B: Environ.*, **2014**, 147, 779-788.
32 J. Zhang, Q. Kang, Z. Yang, H. Dai, D. Zhuang and P. Wang, *J. Mater. Chem. A*, **2013**, 1, 11623-11628.
33 H. L. Wang, J. M. Yan, Z. L. Wang, S-II. O and Q. Jiang, *J. Mater. Chem. A*, **2013**, 1, 14957-14962.
34 N. Cao, L. Yang, C. Du, J. Su, W. Luo and G. Cheng, *J. Mater. Chem. A*, **2014**, 2, 14344-14347.
35 Y. Du, J. Su, W. Luo, G. Cheng, *ACS Appl. Mater. Interfaces*, **2015**, 7, 1031-1034.
36 S. K. Singh, Q. Xu, *J. Am. Chem. Soc.*, **2009**, 131, 18032-18033.
37 D. C. Zhong, K. Aranishi, A. K. Singh, U. B. Demirci and Q. Xu, *Chem. Commun.*, **2012**, 48, 11945-11947.
38 X. Wang, D. Liu, S. Song, H. Zhang, *Chem. Eur. J.*, **2013**, 19, 8082-8086.
39 Y. J. Xu, N. Zhang, *Chem. Mater.*, **2013**, 25, 1979-1988.
40 X. Wang, D. Liu, S. Song and H. Zhang, *J. Am. Chem. Soc.*, **2013**, 135, 15864-15872.
41 A. Hornés, M. J. Escudero, L. Daza, A. Martínez-Arias, *J. Power Sources*, **2014**, 249, 520-526.
42 F. Zhu, G. Chen, S. Sun and X. Sun, *J. Mater. Chem. A*, **2013**, 1, 288-294.
43 A. S. P. Lovón, J. J. Lovón-Quintana, G. I. Almerindo, G. P. Valença, M. I. B. Bernardi, V. D. Araújo, T. S. Rodrigues, P. A. Robles-Dutenhefner and H. V. Fajardo, *J. Power Sorces*, **2012**, 216, 281-289.
44 X. Wang, D. Liu and S. Song, H. Zhang, *J. Am. Chem. Soc.*, **2013**, 135, 15864-15872.
45 M. I. Kim, K. S. Park and H. G. Park, *Chem. Commun.*, **2014**, 50, 9577-9580.
46 L. He, B. Liang, L. Li, X. Yang, Y. Huang, A. Wang, X. Wang and T. Zhang, *ACS Catal.*, **2015**, 5, 1623-1628.
47 Z. Zhang, Y. Wang, X. Chen and Z.H. Lu, *J. Power Sources*, **2015**, 291, 14-19.
48 Y. Yang, Z.H. Lu, Y. Hu, Z. Zhang, W. Shi, X. Chen and T. Wang, *RSC Adv.*, **2014**, 4, 13749-13752.
49 N. I. Kovtyukhova, P. J. Ollivier, B. R. Martin, T. E. Mallouk, S. A. Chizhik, E. V. Buzaneva and A. D. Gorchinskiy, *Chem. Mater.*, **1999**, 11, 771-778.
50 Z. Zhang, Z. H. Lu and X. Chen, *ACS Sustainable Chem. Eng.*, **2015**, 3, 1255-1261.
51 Q. Yao, Z. H. Lu, Z. Zhang, X. Chen and Y. Lan, *Sci. Rep.*, **2014**, 4, 7597; DOI: 10.1038/srepo7597.
52 J. Liu, W. Tang, T. Shen, Z. Zhao, H. Feng, F. Cui, *RSC Adv.*, **2014**, 4, 30624-30629.
53 J. Wang, X. B. Zhang, Z. L. Wang, L.M. Wang, Y. Zhang, *Energy Environ. Sci.*, **2012**, 5, 6885-6888.
54 J. P. Rourke, P. A. Pandey, J. J. Moore, M. Bates, I. A. Kinloch, R. J. Young and N. R. Wilson, *Angew. Chem. Int. Ed.*, **2011**, 123, 3231-3235.
55 D. X. Yang, A. Velamakanni, G. Bozoklu, S. Park, M. Stoller, R. D. Piner, S. Stankovich, I. Jung and D. A. Field, *Carbon*, **2009**, 47, 145-152.
56 S. Stankovich, D. A. Dikin, R. D. Piner, K. A. Kohlhaas, A. Kleinhammes, Y. Y. Jia, Y. Wu, S. T. Nguyen and R. S. Ruoff, *Carbon*, **2007**, 45, 1558-1565.
57 X. Liu, K. Zhou, L. Wang, B. Wang and Y. Li, *J. Am. Chem. Soc.*, **2009**, 131, 3140-3141.
58 X. B. Zhang, J. M. Yan, S. Han, H. Shioyama, Q. Xu, *J. Am. Chem. Soc.*, **2009**, 131, 2778-2779.
59 D. G. Tong, W. Chu, P. Wu, G. F. Gu, L. Zhang, *J. Mater. Chem. A*, **2013**, 1, 358-366.
60 D. G. Tong, W. Chu, P. Wu, L. Zhang, *RSC Adv.*, 2012, **2**, 2369-2376.

Graphical abstract

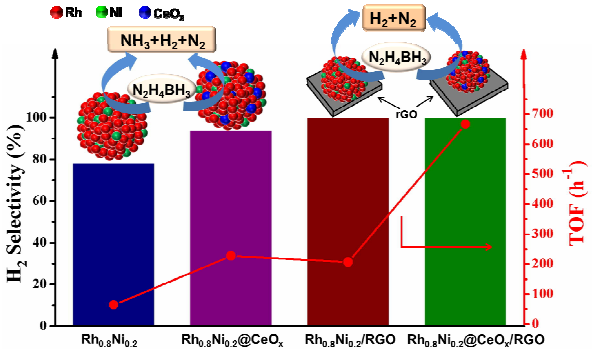

Amorphous CeO_x-doped Rh-Ni NPs grown on reduced graphene oxide nanosheets have been used as highly efficient and recyclable catalysts for complete hydrogen generation from aqueous solution of $N_2H_4BH_3$ or N_2H_4.